



# The Rationale for E2020 as a Potent Acetylcholinesterase Inhibitor

Yoshiyuki Kawakami,<sup>a,\*</sup> Atsushi Inoue,<sup>a</sup> Takatoshi Kawai,<sup>a</sup> Misako Wakita,<sup>a</sup> Hachiro Sugimoto<sup>a</sup> and Anton J. Hopfinger<sup>b,\*</sup>

<sup>a</sup>*Tsukuba Research Laboratories, Eisai Co., Ltd., 1-3, Tokodai 5-chome, Tsukuba-shi, Ibaraki 300-26, Japan*

<sup>b</sup>*Department of Medicinal Chemistry and Pharmacognosy, MC 781, The University of Illinois at Chicago, 833 South Wood Street, Chicago, IL 60612-7231, U.S.A.*

**Abstract**—The phase III drug-candidate, E2020, developed for treatment of Alzheimer's disease, and possibly other dementias, and its analogues have been the focus of extensive molecular pharmacological and structural studies. The potency and selectivity of E2020 as an inhibitor of acetylcholinesterase, AChE, in the brain is established. A combination of molecular modeling and QSAR studies have been used throughout the evolution of the AChE inhibitor program leading to the benzylpiperidine series, and, ultimately, E2020. QSAR studies have identified requirements to optimize inhibition activity as a function of substituent choice on both the indanone and benzyl rings in the E2020 class of inhibitors. A combination of X-ray crystal structure studies of E2020 isomers and the molecular shape analysis, MSA, of E2020 and its analogues has led to a postulated active conformation, and molecular shape, for these AChE inhibitors. The active molecular shape corresponds to a high degree of shape similarity between the two E2020 isomers which, in turn, is consistent with the observed high inhibition potencies of both of these compounds. Intermolecular docking studies were carried out for E2020 and some analogues with the crystal structure of AChE when it became available. The docking simulations involving E2020 analogues suggest these inhibitors do not bind at the acetylcholine, ACh, active site, but rather at the most narrow location of the long channel leading to the active site. Intermolecular binding geometries are consistent with the postulated active conformations derived from structure–activity (receptor geometry independent) information. Copyright © 1996 Elsevier Science Ltd

## Introduction

The reversible acetylcholinesterase (AChE) inhibitor, E2020 (1-benzyl-4-[5,6-dimethoxy-(1-indanone)-2-yl]-methylpiperidine hydrochloride), see Figure 1, has been under clinical study as a candidate drug for the treatment of Alzheimer's disease (AD) where the cholinergic function is selectively, and irreversibly, affected in this senile dementia disease.<sup>1</sup> The mechanism proposed to explain the memory improvement through AChE inhibition is an increase in acetylcholine (ACh) levels in the central cholinergic synapses involved in the memory circuit.<sup>2–5</sup>

In principle, the synthesis of acetylcholine, its terminal release, interaction with synaptic receptors and ultimate degradation are straightforward mechanisms although the biochemical picture at each of these levels is becoming increasingly complex. Figure 2 shows a simplified metabolic pathway related to acetylcholine. The cholinergic hypothesis postulates that memory impairments in patients with AD result from a deficit of cholinergic functions in the brain. Several neurotransmitter systems undergo changes with advanced age. Significant cholinergic dysfunctions can occur in an aged and demented central nervous system. With respect to acetylcholine synthesis, it is generally accepted that the immediate precursors, acetyl coenzyme A and choline, are ultimately derived from circulating blood glucose and choline, respectively.<sup>6</sup>

Activity of cholinergic markers, such as choline acetyltransferase and choline uptake, are markedly reduced (at least 40%) in the brains of patients with AD in comparison to age-matched controls. Biopsies indicate that cortical choline acetyltransferase loss can occur in AD, and certain areas, including the hippocampus, are most severely biochemically affected.

There exist relationships between the changes described above and loss of memory. Similar memory deficits can also be artificially induced by blocking cholinergic mechanisms in young subjects. Consequently, potentiation of central cholinergic action has been proposed as an approach for the palliative treatment of mild to moderate cases of AD.

The cholinergic hypothesis has provided the first rational approach to the treatment of AD by neurotransmitter replacement. ACh precursors, including various preparations of choline and lecithin, were the first compounds administered in the treatment of AD in an attempt to augment central cholinergic activity by enhancing ACh levels. However, the results of clinical studies have, so far, shown little or no evidence for the efficacy of this approach. AChE inhibitor type of drugs do show improvements in cognitive function in clinical study. Cholinergic agonists acting directly on muscarinic receptors may improve the cholinergic dysfunction. Five genetically defined muscarinic receptors subtypes (m1–m5) have been reported to date.<sup>7</sup>

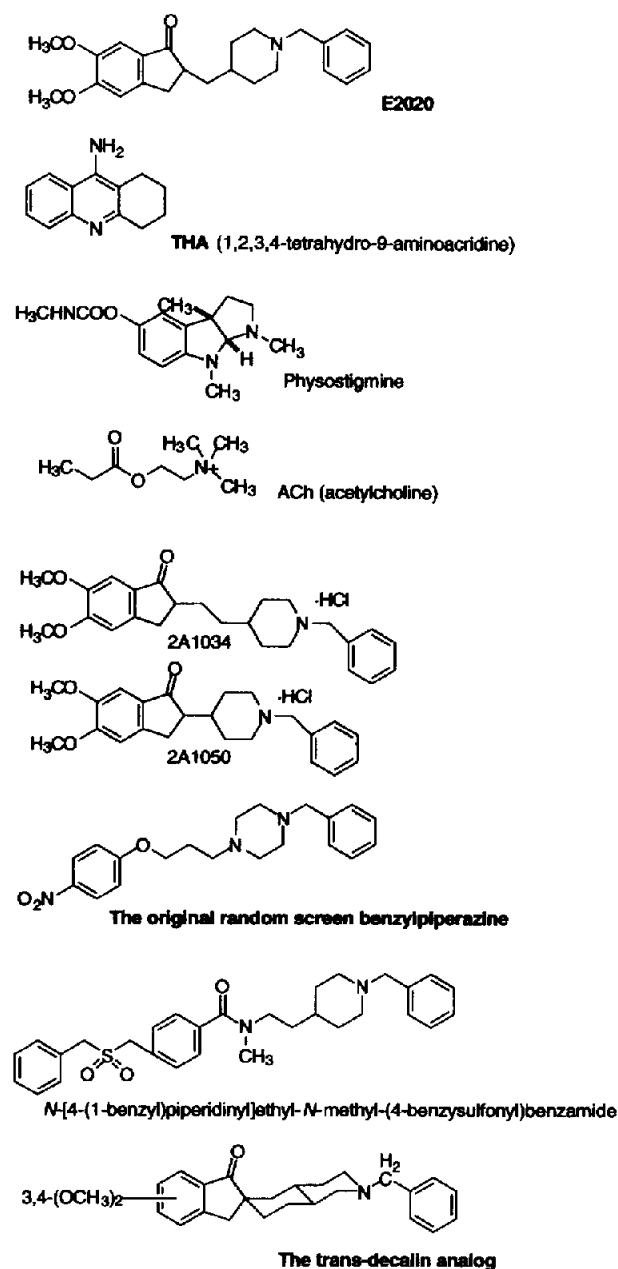


Figure 1. Structure of AChE inhibitors.

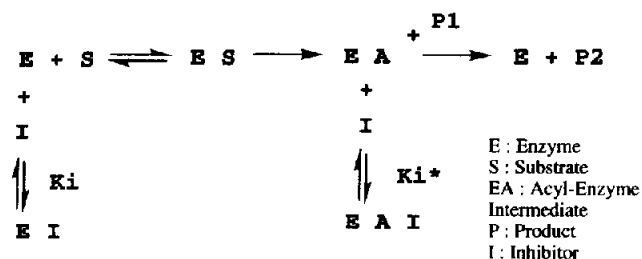


Figure 2. Reaction scheme in which the inhibitor combines with AChE and acylated AChE. E, free enzyme; S, substrates; ES, enzyme substrate complex; EA, acylated enzyme; P, product; I, inhibitor; ES, enzyme inhibitor complex; EA·I, acylated enzyme inhibitor complex;  $K_i$ , dissociation constant for enzyme and inhibitor;  $K_i^*$ , dissociation constant for EA and inhibitor.

E2020 is the lead compound in a new class of AChE inhibitors having an *N*-benzylpiperidine and an indanone moiety which shows a greater selectivity for AChE than for butyrylcholinesterase, and is not expected to have any peripheral effects.<sup>8</sup> E2020 has been developed as a racemic mixture due to the same inhibitory profiles from each of the enantiomers.<sup>9</sup> Clinical studies of E2020 suggest that it is possibly effective in the treatment of patients with AD.<sup>10</sup> THA (tetrahydroaminoacridine, Fig. 1) recently became the first available agent for the treatment of AD in the U.S. However, the aminoacridines, in general, suffer from dose-limiting hepatotoxicity which is believed to be structure related.<sup>11</sup> Physostigmine, a carbamate-type inhibitor, has shown inconclusive results in the clinic, perhaps due to its short half-life and narrow therapeutic index. A controlled-released formulation of physostigmine is currently in phase-III trials. E2020 appears to be devoid of such an unfavorable side-effect profile probably because of its novel benzylpiperidine structure. Many groups have undertaken the design and synthesis of E2020-like compounds which incorporate bioisosteric replacements for the indanone ring.<sup>12,13</sup>

## Methods and Results

### Lead identification and optimization

A benzylpiperazine compound, see Figure 1, demonstrating weak (its  $IC_{50}$  is 14.5  $\mu M$ ), but definite inhibitory activity against AChE was identified in blind screening. Continued screening was performed around compounds of similar structures. Another type of 'seed' compound was found which has both benzylpiperidine and benzamide moieties in its structure. This compound has strong AChE activity, its  $IC_{50}$  being in excess of two orders of magnitude than that of the lead compound. Lead optimization synthesis, mainly involving modification of the benzamide moiety, led to *N*-[4-(1-benzyl)piperidinyl]ethyl-*N*-methyl-(4-benzylsulfonyl)benzamide, see Figure 1, which has an AChE  $IC_{50}$  five orders of magnitude smaller (higher inhibition potency) as compared to the original benzylpiperazine compound, as well as selective AChE inhibitory activity. However, compound 1 has a very short half-life due to hydrolyzation by proteases in the liver, which is believed to lead to an *N*-disubstituted amide metabolite.

Metabolic resistance was sought by incorporating bioisosteric replacements for the *N*-disubstituted amide moiety. A series of benzamide analogues possessing high AChE activity and which are readily transported into brain became the focus in the lead optimization process.

Over the course of the lead optimization it appeared that methyl substitution on the amide nitrogen enhanced activity. Thus, *trans* and *cis* forms of benzamide were considered as models since methyl substitution at the amide nitrogen may change the ratio of *cis* and *trans* isomers of the amide. Overall, conformation

$$\log 1/C = 0.019 MR - 2.372 \Delta E(C-T) + 22.94$$

$$n=19, s=0.256, r=0.833$$

log 1/C : negative logarithm of IC<sub>50</sub> of AChE  
 MR : molar refractivity  
 $\Delta E(C-T)$  : energy difference between *cis* and *trans* isomer (kcal/mol) by CNDO/2

Figure 3. QSAR of *para*-substituted benzamides.

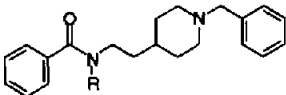
was considered an important component in a QSAR analysis used to guide the initial lead optimization process. A good correlation equation, QSAR, was found between activity, as measured by IC<sub>50</sub>, and the difference in energy between the *cis* and *trans* isomers,  $\Delta E(C-T)$  and the bulkiness of substituents (see Figure 3). The QSAR suggests that the intrinsic activity of *cis* isomers of benzamide are higher than the *trans* isomers, since there is a negative correlation between IC<sub>50</sub> and  $\Delta E(C-T)$ .

Table 1 contains the structure–activity behavior of *N*-alkylated amides which have higher activity compared with non-*N*-alkylated analogues. Conformational analysis of the *N*-alkyl-substituted benzamides was performed using the MNDO quantum chemical method.<sup>14</sup> Figure 3 contains the estimated ratio of *trans* and *cis* isomers of some *N*-alkyl substituted benzamides. Nonsubstituted amides exist almost completely in the *trans* form, but *N*-substitution raises the *trans* conformational energy state so that, overall, the *cis* conformation becomes more stable. These results again indicate that AChE activity increases as the population of the *cis* isomer of the benzamide increases.

The QSAR analysis provided the structural requirements for lead evolution. The specific structural requirements identified in the QSAR analysis are as follows: (1) the *cis* conformation of the benzamide is the active conformation, (2) bulky groups at the *para* position of the benzamide increases activity, and (3) the carbonyl oxygen of the amide is a proton acceptor for an intermolecular hydrogen bond.

Flexible benzamide analogues having the *cis* conformation were made. One of these was E2020 which

Table 1. *N*-Alkyl analogues of *N*-[4-(1-benzyl)piperidinyl]ethylbenzamide



R	IC <sub>50</sub> (mM)
H	560
Benzyl	180
Methyl	170
Ethyl	130
Phenyl	35

possesses benzylpiperidine and indanone moieties. E2020 was the first compound in which an indanone ring was part of the enzyme inhibitor.

### E2020 as a selective AChE inhibitor

**Pharmacology.** E2020 was initially thought to be a mimic of ACh by structural similarity, and, therefore, a competitive inhibitor of AChE. The *N*-benzylpiperidines show outstanding in vitro selectivity for AChE. The IC<sub>50</sub> of E2020 for AChE is 5.7 nM, while the IC<sub>50</sub> for BuChE (butyrylcholinesterase) is ~7000 nM, a selectivity ratio in excess of three orders of magnitude. THA and physostigmine show poor selectivity having the same order of magnitude IC<sub>50</sub>s for both AChE and BuChE. Inhibition of BuChE, which is abundant in plasma, may be associated with potentiating peripheral side effects.<sup>15</sup> Therefore, an AChE inhibitor which is essentially devoid of BuChE activity may display higher therapeutic indices than those which are also active BuChE inhibitors.

**Dissociation constants.** AChE catalysis involves an active serine residue, and the overall catalytic process proceeds in a three-step mechanism, as defined in Figure 2, like transfer within a catalytic triad. The activated serine residue enables a nucleophilic attack on ACh, resulting in hydrolysis and acetate products being released. Some reversible AChE inhibitors show a mixed type of inhibition by blocking the deacetylation process. The acetyl group is introduced into the esteratic site in this catalytic process. Therefore, acylated AChE can accept an external charged molecule at this vacant anionic site to form an EA–inhibitor complex (EAI). E2020 appears to bind to both the free enzyme and the acylated enzyme to block both Michaelis complex formation and deacetylation.

### Molecular modeling and lead evolution

**X-ray crystallography of E2020.** A single crystal of E2020, crystallized from ethanol:acetone (1:2) mixed

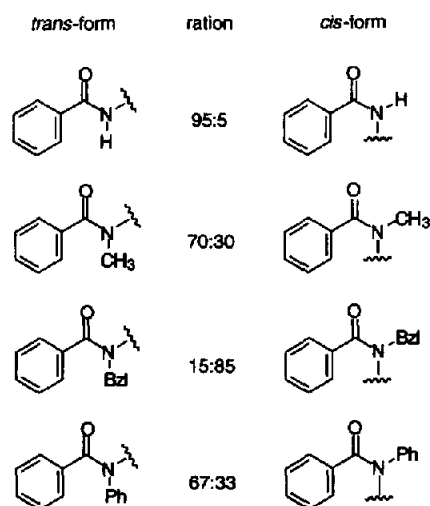


Figure 4. Estimated ratio of *trans* and *cis* isomer 5 in *N*-alkyl analogues of *N*-[4-(1-benzyl)piperidinyl]ethylbenzamide.

solution, was prepared and used. Data collection was performed with Cu  $K\alpha$  radiation ( $\lambda=1.54184$  Å) on an Enraf–Nonius CAD4 computer-controlled  $k$  axis diffractometer equipped with a graphite crystal, incident beam monochromator. The crystal was found to be triclinic with unit cell parameters  $a=9.977$  (2),  $b=13.347$  (4),  $c=8.541$  (6) Å,  $\alpha=92.72$  (4)°,  $\beta=100.59$  (3)°,  $\gamma=75.47$  (2)°, and  $V=1082.1$  Å<sup>3</sup>. For  $Z=2$  and  $M_r=415.96$ , the calculated density  $D_{\text{calc}}$  is 1.28 g/cm<sup>3</sup>. From least-squares refinement, the space group was determined to be  $P1$  (No. 2). The data were collected to a maximum  $2\theta$ - $\omega$  of 128.0° using the  $2\theta$ - $\omega$  scan technique. Lorentz and polarization corrections were applied to the data. No absorption correction was made and intensities of equivalent reflection were averaged. The structure was solved by direct methods. Full-matrix least-squares refinement of atomic positional and thermal parameters [anisotropic C, Cl, N, O; isotropic H (fixed at 4.0 Å<sup>2</sup>)] converged at  $R=0.073$  over 2818 reflections with  $I>3\sigma(I)$ .

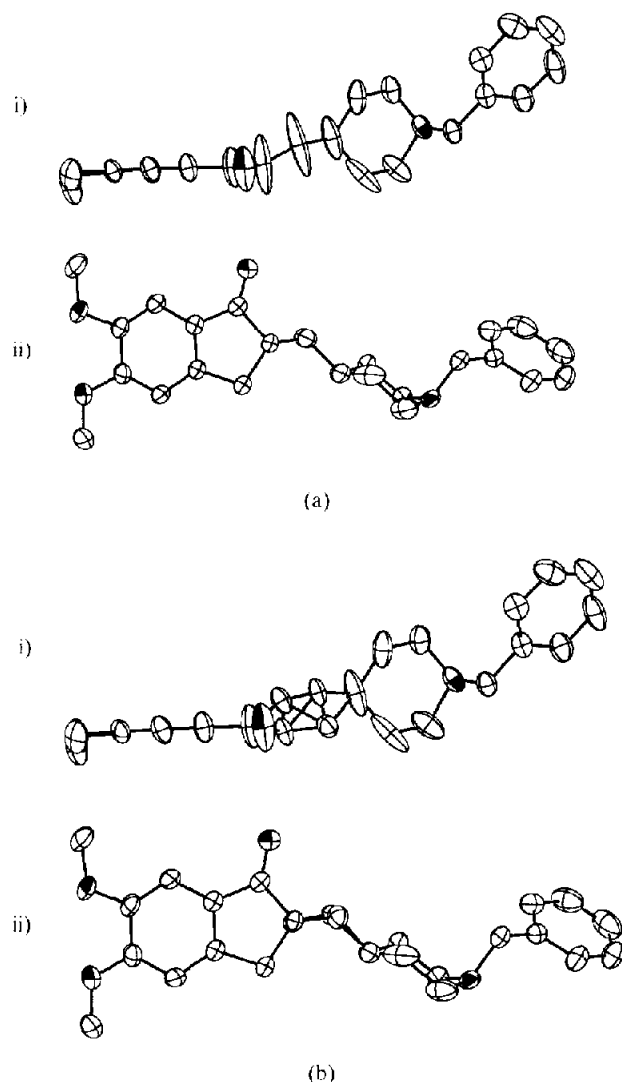
The same procedures used to determine the crystal structure of E2020 at ambient temperature were also employed to solve the crystal structure of E2020 at low temperature (−20 °C). The unit-cell parameters were  $a=9.982$  (5),  $b=13.335$  (7),  $c=8.526$  (5) Å,  $\alpha=92.38$  (4)°,  $\beta=100.71$  (5)°,  $\gamma=75.38$  (4)°, and  $V=1079.0$  Å<sup>3</sup>,  $Z=2$  and  $D_{\text{calc}}$  is 1.28 g/cm<sup>3</sup>. The space group is  $P1$ ;  $2\theta=128.0^\circ$ . Thermal parameters were refined anisotropically for C, Cl, N, O and isotropically for H. The final  $R$  value is 0.075 over 3120 reflections with  $I>3\sigma(I)$ .

Figure 5 shows the ORTEP<sup>16</sup> drawing of the racemic E2020 crystal structure. The ORTEP shows a pattern of irregular thermal ellipsoids. There is an asymmetric carbon atom at the 2-position of indanone ring and the irregular thermal motions phenomenon occurs around this chiral center. This thermal behavior is observed both at 23 and −20 °C and corresponds to two puckering structures of the indanone ring. Thus, the crystal structure of the indanone ring consists of two conformers. One conformer has a relative  $R$  configuration and the other has a relative  $S$  configuration. The most remarkable feature of  $R$  and  $S$  enantiomers is that they have the same molecular-shape except for small portions of the indanone and piperidine rings. The  $R$  and  $S$  configurations are so similar that they are not even recognized in the crystalline state. These two conformers also have almost equal heats of formation as computed by MNDO, and the crystal structure is one of the most stable intramolecular conformations of each E2020 enantiomer. This high intramolecular stability suggests that these two conformations may not only exist in the crystal state, but also in solution. However, solution structure studies of E2020 have not yet been performed.

**Receptor independent molecular modeling and QSAR analyses.** A comprehensive computer-assisted molecular design, CAMD, investigation of some of the E2020 analogues began at a point where crystals structures of E2020 had been determined, but a crystal

structure of a AChE was not yet available. Approximately 80 analogues of E2020 had also been made and tested at the start of the on-going comprehensive CAMD study, and somewhere between 25 and 35 additional analogues have become available over the course of the CAMD investigation to date. This CAMD study is continuing with a focus on inter-molecular ligand–receptor modeling.

The experimental design phase of the CAMD study identified that the maximum amount of structure–activity information would be derived from using only those analogues that could be placed into one of four structural feature sets. Each structural feature set corresponds to analogues differing from one another by a single, common location chemical change. This permits the differences in activity for analogues in a set to be considered only a function of the single chemical



**Figure 5.** (a) X-ray crystal structure of racemic E2020 at −20 °C. (i, top) View along the plane of the indanone ring. (ii, bottom) View into the plane of the indanone ring. (b) X-ray crystal structure of racemic E2020 for discrete peaks. A racemic occupancy of 0.6( $R$ ) and 0.4( $S$ ) was found from the differential Fourier map. (i, top) View along the plane of the indanone ring. (ii, bottom) View into the plane of the indanone ring.

modification characteristic of the set. The composite experimental design led to the consideration of all E2020 analogues of the structural class shown in Figure 6. Within the framework of CAMD methods the construction of the four *feature* sets defined in Figure 6 corresponds to using the molecular decomposition–recomposition, MDR, technique<sup>17</sup> to construct databases for combined QSAR and molecular modeling studies on indanone benzyl piperidine inhibitors of AChE. The justification of using the particular MDR operation defined in Figure 6 is given in ref 18. The CAMD study for each feature is described below.

**Feature 1.** The set of 17 analogues reported in Table 2 were used to develop the feature 1 QSARs. These compounds were selected because all of them have the same general structure, **I**. The feature 1 structures differ from one another only by the substituents ( $R_1$ ,  $R_2$ ,  $R_3$ ) on the aromatic ring of the indanone bicycle. Thus, the SAR for this set of compounds is due only to ( $R_1$ ,  $R_2$ ,  $R_3$ ), and the MDR technique can be applied. In general, isomers at the \*-carbon of the indanone ring are not resolved with respect to inhibition potency. The role of this chiral center on molecular conformation has been explored as part of the feature 2 analysis. The spacer link from C\* to the piperidine ring is at least partially saturated, and in most cases totally saturated, so that resonance effects from substituent modifications on the rest of the molecule can be neglected.

The range on AChE inhibition potency for the 18 analogues is 1.3–380 nM  $IC_{50}$  units.

Conformational and electronic descriptors were determined using the model compound **I** to represent all analogues. The details of the molecular modeling procedures are given in ref 18.

Local minimum energy conformer states up to 6 kcal/mol above the apparent global minimum<sup>19</sup> were used to generate property measures of the descriptors used to generate feature 1 trial QSARs. The following set of descriptors was used in the QSAR analysis of feature 1: (1) Partial charge densities (from MNDO) on the  $C_1$  to  $C_6$  carbon atoms in **3**. (2) The total dipole moment,  $U_T$ , and the angle the dipole makes with the  $C=O$  bond in the plane of the indanone ring. (3) Component of the dipole moment in the  $C=O$  direction,  $U_Z$ . (4)

Lowest unoccupied molecular orbital energy, LUMO. (5) Highest occupied molecular orbital energy, HOMO. (6) Atomic orbital electron populations in  $C_3$ ,  $C_4$ , and  $C_5$ . (7) Sum of the atomic orbital electron populations in  $C_1$ – $C_6$ . (8) Sum of the atomic orbital electron populations in  $C_1$ – $C_6$  plus  $C_9$  and  $O_{10}$ . HOMO  $\pi$  coefficient of each of the phenyl carbons  $C_1$ – $C_6$  as well as  $O_{10}$ . (10) Sum of the squares of the HOMO  $\pi$  coefficients of  $C_1$ – $C_6$  plus  $C_9$  and  $O_{10}$ . (11) Partition coefficient,  $\log P$ ,<sup>20</sup> of **X 3**.

Trial QSARs were generated by considering all combinations of the descriptors for feature 1. Both linear and quadratic descriptor terms were used in the set of multidimensional linear regression, MLR, analyses. The SAS package<sup>21</sup> was used to carry out the statistical analyses.

### GA discussion

The optimum 3-D QSAR that could be constructed using direct MLR for substitution onto the aromatic unit of the indanone ring, based upon all of the analogues in Table 2, is:

$$-\log(IC_{50}) = 2.73[C_4] + 1.86[U_T] - 0.14[U_T^2] - 156.7[HOMO] - 8.25[HOMO^2] - 740.93 \quad (1)$$

$N=17$ ;  $R=0.804$ ;  $SD=0.46$ ;  $F=4.4$ ;  $U_T(\max)=6.6$  debye;  $HOMO(\max)=-9.49$  eV,

where  $C_4$  is the HOMO out-of-plane  $\pi$ -orbital coefficient of ring carbon four, and the other terms in equation (1) have already been explicitly defined. An analysis of the residual of fit,  $\Delta \log(IC_{50}) = (-\log(IC_{50}))_{\text{obsd}} - (-\log(IC_{50}))_{\text{calcd}}$ , of equation (1) indicates that the marginal fit of this correlation equation is largely due to two outliers—compounds **4** and **17** of Table 2. Compound **4** is predicted to be less active than observed, while the opposite is true for **17**.

If compounds **4** and **17** are not considered in the direct MLR analysis, then the remaining 15 compounds can be described by the 3-D QSAR:

$$-\log(IC_{50}) = 2.21[C_4] - 6.65[U_T] + 1.18[U_T^2] - 162.9[HOMO] - 8.58[HOMO^2] - 757.52 \quad (2)$$

$N=15$ ;  $R=0.939$ ;  $SD=0.25$ ;  $F=14.8$ ;  $U_T(\max)=2.8$  debye;  $HOMO(\max)=-9.49$  eV.

The most obvious difference between equations (1) and (2), besides the considerable increase in statistical

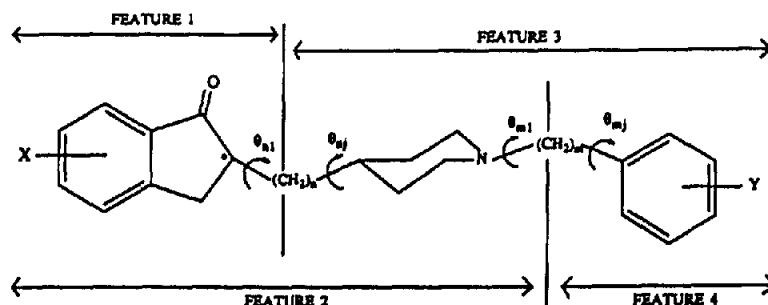
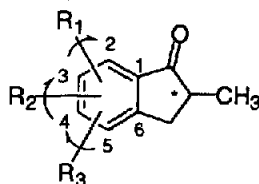


Figure 6. Definition of the four features of the E2020 analogue inhibitors of AChE.

Table 2. General SAR data for Feature I based upon model compound I



No.	R <sub>1</sub>	R <sub>2</sub>	R <sub>3</sub>	C <sub>4</sub>	U <sub>T</sub>	HOMO energy (debye) (eV)	Obsd -log (IC <sub>50</sub> )	Calcd [equation (2)] -log (IC <sub>50</sub> )	Obsd-calcd [equation (1)] -log (IC <sub>50</sub> )	Calcd [equation (2)] -log (IC <sub>50</sub> )	Obsd-calcd [equation (2)] -log (IC <sub>50</sub> )
1	3-OH	4-OMe	H	0.356	3.918	-9.305	8.88	8.46	0.42	8.81	0.07
2	3-OMe	4-OMe	H	0.454	2.301	-9.533	8.28	7.38	0.90	8.20	0.08
3	3-OEt	4-OEt	H	0.505	2.855	-9.631	8.20	8.00	0.20	7.86	0.34
4	H	H	5-Me	0.234	2.966	-9.593	8.15	7.46	0.69		
5	3-OMe	4-O-isop	H	0.449	3.332	-9.451	8.05	8.48	-0.43	8.19	-0.14
6	H	H	5-OMe	0.249	3.127	-9.545	7.92	7.72	0.20	7.55	0.37
7	2-OMe	3-OMe	4-OMe	0.468	2.765	-9.615	7.88	7.84	0.04	7.82	0.06
8	H	4-OMe	5-OMe	0.452	2.629	-9.461	7.70	7.77	-0.07	7.93	-0.23
9	3,4-Methylenedioxy		H	0.409	2.785	-9.314	7.64	7.58	0.06	7.51	0.13
10	2-OMe	4-OMe	H	0.364	2.845	-9.581	7.60	7.70	-0.10	7.64	-0.04
11	2-OMe	H	5-OMe	0.251	3.248	-9.443	7.44	7.86	-0.42	7.65	-0.21
12	3-Me	H	H	0.168	3.004	-9.615	7.16	7.27	-0.11	7.19	-0.03
13	3-OMe	H	H	0.247	2.980	-9.577	7.09	7.53	-0.44	7.42	-0.33
14	2-OMe	3-OMe	H	0.027	3.192	-9.376	7.06	7.10	-0.04	7.00	0.06
15	H	H	H	0.021	3.009	-9.716	6.83	6.58	0.25	6.58	0.25
16	3-F	H	H	0.226	3.467	-9.856	6.70	6.90	-0.20	6.80	-0.10
17	3-OMe	4-OH	H	0.463	1.946	-9.508	6.42	6.97	-0.55		

significance of equation (2), is the change in the dependence of  $-\log(\text{IC}_{50})$  on  $U_T$ . According to equation (2),  $-\log(\text{IC}_{50})$  increases with increasing  $U_T$  for  $U_T > 2.8$  debye, while for equation (1),  $-\log(\text{IC}_{50})$  decreases as  $U_T$  increase for  $U_T > 6.6$  debye. However, these two relationships between  $-\log(\text{IC}_{50})$  and  $U_T$  are not inconsistent for most of the analogues in Table 2. Fifteen of the 17 compounds in Table 2 have  $U_T$  values in the 2.8–6.6 debye range. Both equations (1) and (2) predict  $-\log(\text{IC}_{50})$  to increase with increasing  $U_T$  in this range of dipole values.

Neither equations (1) or (2) are particularly satisfying. Consequently, a subsequent QSAR analysis was undertaken using a genetic algorithm formalism called the genetic function approximation, GFA.<sup>22</sup> The GFA algorithm applied to the feature 1 dataset illustrates the automatic behavior of spline-based models in QSAR analysis.<sup>23</sup>

Feature 1 QSAR analysis using the GFA began with a population of 300 random models. The terms of the models were linear polynomials, linear splines, and quadratic splines. Only the three descriptors identified in the MLR study were used. However, spline basis functions were included to explore possible partitions of the data set. The population was evolved for 5000 crossover operations. By that point there was little continued improvement in the average score of the models in the population.

The splines used are *truncated power splines* and are denoted with angle brackets. For example,

$\langle f(x) - a \rangle$  is equal to zero if the value of  $(f(x) - a)$  is negative, else it is equal to  $(f(x) - a)$ . The constant  $a$  is termed the *knot* of the spline. When a spline term is created, the knot is set using the value of the descriptor in a random data sample.

Splines are interpreted as performing either *range identification* or *outlier removal*. If there are many members in the nonzero partition, then the spline is identifying a range of effect. If there are only a few members of the nonzero set, the spline is identifying outliers. Regression can use the spline term to fit these members independent of the other terms of the model by, effectively, making them 'special cases' based on the extreme value of a descriptor.

The top 10 QSAR models discovered by the GFA algorithm are reported in Table 3. An example of outlier removal is the most frequent used spline,  $\langle 2.301 - U_T \rangle$ . The only compound for which this item is nonzero is compound 17, which was identified as one of the two outliers in the original study. All of the top 10 models isolate compound 17 in this manner. An example of range identification is the use of spline terms based on HOMO. For example, model 3 contains the term  $\langle -9.545 - \text{HOMO} \rangle^2$ , which is nonzero for approximately half of the compounds: 3, 4, 7, 10, 12, 13, 15, and 16. The interpretation is the HOMO has an effect on activity only after it achieves a more negative value than  $-9.545$ . Four of the top 10 most frequently used basis functions are of this form.

An interesting effect in the selection of splines for the top 10 QSAR models was the isolation of the least

active compounds. If a histogram is constructed of the number of times each spline term is nonzero for each of the compounds in the data set, a strong skew toward the least active compounds is observed, as shown in Figure 7. The system is building general models of the most-active compounds and taking the least-active as special cases.

**Feature 2.** The set of model compounds encompassed in II was used to characterize the conformational behavior of the bicycle-piperidine portion of the AChE inhibitor analogues. In II,  $W = (CH_2)_n$  [ $n = 0, 1, 2$ , or  $3$ ], or a combination of single and double bond spacer units,  $A$  is usually  $CH_2$ , but can also be  $C=O$ , and  $X$  and  $Y$  are  $CH$  or  $N$ .

Table 4 contains the set of substructure II analogues used to investigate feature 2. Each structure in Table 4 corresponds to an analogue of E2020 for which the remainder of the molecule  $CH_2Ph$  is replaced by  $Me$ .

Thus, the variations in  $IC_{50}$  reported in Table 4 are due solely to the structural changes represented by II. Note that a couple of key analogues in Table 4, with respect to modeling, correspond to changes on the piperidine ring of E2020: (1) compound **20** in which there is an additional nitrogen atom at position  $X$  and (2) compound **21** in which the piperidine nitrogen has been changed from  $Y$  to  $X$ . Table 4 is subdivided into (a) that contains active inhibitors which have one or two torsion angles ( $\theta_1, \theta_2$ ) between the bicycle and the piperidine rings, (b) that contains substructure analogues for inactive inhibitors having zero, one, or two torsion angles between the rings, (c) that contains substructure analogues for active inhibitors having three or four torsion angles between the rings. It should be noted that some 6–6 bicycles were considered in exploring the SAR and one is given in Table 4. These analogues provide additional information to map the active molecular shape of feature 2 substructures.

**Table 3.** The top 10 3-D QSAR models derived for feature 1 based upon GFA analysis

<p>(1) <math>-\log (IC_{50}) = 6.950</math>  <math>+2.046^* C_4</math>  <math>-6.523^* &lt;2.301 - U_i&gt;</math>  <math>+1.037^* (U_i - 2.845)^2</math>  <math>-22.090^* &lt;-9.631 - HOMO&gt;^2</math>            LOF: 0.209  <math>r</math>: 0.923  <math>F</math>: 17.16</p>	<p>(6) <math>-\log (IC_{50}) = 7.138</math>  <math>-1.615^* &lt;C_4 - 0.027&gt;</math>  <math>-7.619^* &lt;2.301 - U_i&gt;</math>  <math>+1.231^* (U_i - 2.966)^2</math>  <math>-4.616^* &lt;-9.631 - HOMO&gt;</math>            LOF: 0.225  <math>r</math>: 0.917  <math>F</math>: 15.80</p>
<p>(2) <math>-\log (IC_{50}) = 7.101</math>  <math>+2.040^* C_4</math>  <math>-4.581^* &lt;2.301 - U_i&gt;</math>  <math>+2.988^* &lt;U_i - 3.467&gt;</math>  <math>-7.178^* (HOMO + 9.508)^2</math>            LOF: 0.216  <math>r</math>: 0.920  <math>F</math>: 16.55</p>	<p>(7) <math>-\log (IC_{50}) = 7.092</math>  <math>+1.756^* &lt;C_4 - 0.027&gt;</math>  <math>-7.667^* &lt;2.301 - U_i&gt;</math>  <math>+1.234^* (U_i - 2.966)^2</math>  <math>-15.250^* &lt;9.593 - HOMO&gt;^2</math>            LOF: 0.225  <math>r</math>: 0.917  <math>F</math>: 15.79</p>
<p>(3) <math>-\log (IC_{50}) = 7.053</math>  <math>+1.983^* &lt;C_4 - 0.027&gt;</math>  <math>-6.468^* &lt;2.301 - U_i&gt;</math>  <math>+0.987^* (U_i - 2.845)^2</math>  <math>-11.185^* &lt;-9.545 - HOMO&gt;^2</math>            LOF: 0.221  <math>r</math>: 0.918  <math>F</math>: 16.10</p>	<p>(8) <math>-\log (IC_{50}) = 7.098</math>  <math>+1.607^* C_4</math>  <math>-7.615^* &lt;2.301 - U_i&gt;</math>  <math>+1.231^* (U_i - 2.966)^2</math>  <math>-4.610^* &lt;-9.631 - HOMO&gt;</math>            LOF: 0.225  <math>r</math>: 0.917  <math>F</math>: 15.78</p>
<p>(4) <math>-\log (IC_{50}) = 7.035</math>  <math>+1.771^* C_4</math>  <math>-7.683^* &lt;2.301 - U_i&gt;</math>  <math>+1.241^* (U_i - 2.966)^2</math>  <math>-18.192^* &lt;-9.615 - HOMO&gt;^2</math>            LOF: 0.224  <math>r</math>: 0.917  <math>F</math>: 15.84</p>	<p>(9) <math>-\log (IC_{50}) = 8.076</math>  <math>-2.110^* &lt;0.468 - C_4&gt;</math>  <math>+3.354^* &lt;U_i - 3.467&gt;</math>  <math>-12.972^* &lt;2.301 - U_i&gt;^2</math>  <math>-8.219^* (HOMO + 9.545)^2</math>            LOF: 0.225  <math>r</math>: 0.916  <math>F</math>: 15.74</p>
<p>(5) <math>-\log (IC_{50}) = 7.080</math>  <math>+1.778^* &lt;C_4 - 0.027&gt;</math>  <math>-7.686^* &lt;2.301 - U_i&gt;</math>  <math>+1.242^* (U_i - 2.966)^2</math>  <math>-18.196^* &lt;-9.615 - HOMO&gt;^2</math>            LOF: 0.224  <math>r</math>: 0.917  <math>F</math>: 15.82</p>	<p>(10) <math>-\log (IC_{50}) = 7.056</math>  <math>+1.739^* C_4</math>  <math>-21.539^* &lt;2.301 - U_i&gt;^2</math>  <math>+1.223^* (U_i - 2.966)^2</math>  <math>-13.468^* &lt;-9.577 - HOMO&gt;^2</math>            LOF: 0.226  <math>r</math>: 0.916  <math>F</math>: 15.65</p>

Active conformations were sought by attempting to identify stable intramolecular conformer states for active analogues that are not stable for inactive analogues. This modeling strategy is called the LBA-LCS (loss in biological activity–loss in conformational stability) principle.<sup>24</sup> The details of the conformational analyses are given in ref 18.

Molecular-shape comparisons were performed by superimposing pairs of molecules under an initial three-atom constraint (spatial pharmacophore) and

then performing an optimization with respect to the molecular-shape similarity measure. The measure of molecular-shape similarity has been based upon considering molecular geometry and corresponding conformational energetics. The geometric measures of molecular shape similarity include one, or more, pairs of interatomic distances and/or maximizing common overlap steric volume. Conformational energetics have been built into the estimation of molecular-shape similarity by using loss in conformational energy of an analogue (relative to the intramolecular global minimum energy conformation), to achieve an increase in the geometric measure of molecular-shape similarity, as a penalty function to the geometric measure.<sup>25</sup>

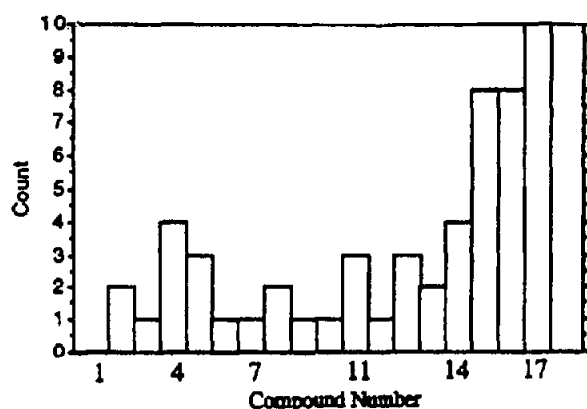


**Figure 7.** Histogram of the number of times a given compound was made a special case in the top 10 models. The histogram shows a skew toward the highest-numbered compounds, which are also the least active. In effect, the GFA algorithm is making special cases of the least-active compounds and modeling the patterns it found in the most active analogues.

The four compounds, two actives, **18A** and **20**, and two inactive, **21** and **22** (of Table 4), whose conformational energy maps are shown in Figures 8 and 9 have a common global minimum near ( $q_1=300$ ,  $q_2=300^\circ$ ). These compounds also have various other local minimum energy regions as can be seen in Figures 8 and 9. At this point, any of the conformations near minima might be the active conformer. However, it is unlikely that any of the high-energy conformer minima of **18A** and **20** in the upper left-hand portion of their respective energy maps could be the active conformation. Hence, conformations ( $\theta_1=300$ ,  $\theta_2=300^\circ$ ) and ( $\theta_1=200$ ,  $\theta_2=200^\circ$ ) are considered the only possible candidates for the active ( $\theta_1$ ,  $\theta_2$ ) conformation.

Conformational analysis of the *trans* isomer of compound **19** the other active analogue of Table 4 (the *cis* isomer was found to be a high-energy isomer for all

**Table 4.** The analogues of, or similar to, E2020 used to map the active conformations, ( $q_1$ ,  $q_2$ ), with respect to feature 2

No.	A	B	C	D	X	Y	W	IC <sub>50</sub> , nM
(a) Active analogues with two torsion angles ( $\theta_1$ , $\theta_2$ )*								
<b>18A</b>	CH <sub>3</sub>	Bond	CH—	CH—O	CH	N		5.3
<b>18B</b>	CH <sub>2</sub>	Bond	CH	C—O	CH	N	—CH <sub>2</sub> —(S)	7.7
<b>19</b>	CH <sub>3</sub>	Bond	C=	C=O	CH	N	=CH—	8.4
<b>20</b>	CH <sub>2</sub>	Bond	CH—	C—O	N	N	—CH <sub>2</sub> —	94.0
(b) Inactive analogues with one, $\theta_1$ , or two torsion angles ( $\theta_1$ , $\theta_2$ )								
<b>21</b>	CH <sub>2</sub>	Bond	CH—	C=O	N	CH	—CH <sub>2</sub> —(R/S)	480.0
<b>22</b>	CH <sub>2</sub>	Bond	—C—	HC—	CH	N	—CH <sub>2</sub> —	4400.0
<b>23</b>	CH <sub>3</sub>	Bond	CH—	C—O	CH	N	(R/S)	3300.0
<b>24</b>	CH <sub>2</sub>	Bond	C—	C=O	=C	N	—	1200.0
(c) Active analogues with three ( $\theta_1$ , $\theta_2$ , $\theta_3$ ) or four torsion angles ( $\theta_1$ , $\theta_2$ , $\theta_3$ , $\theta_4$ )								
<b>25</b>	C=O	Bond	N—	C=O	CH	N		0.90
<b>26</b>	NH	C—O	CH—	C—O	CH	N	—(CH <sub>2</sub> ) <sub>2</sub> —	4.2
<b>27</b>	CH <sub>2</sub>	Bond	CH—	C—O	CH	N		1.5
<b>28</b>	CH <sub>2</sub>	Bond	C=	C=O	CH	N	=CH(CH <sub>2</sub> ) <sub>2</sub> —	0.82
<b>29</b>	CH <sub>3</sub>	Bond	C—	C=O	CH	N		3.0

conformer states), indicates two minimum energy states with respect to  $\theta_2$ .

Superposition of the conformational minima of compound **19**, with the two possible active conformations of **18A**, suggests that the conformer ( $\theta_1=300^\circ$ ,  $\theta_2=300^\circ$ ) of **1A** is the only one which adopts a similar molecular shape to a minimum of **19**. Therefore, the ( $\theta_1=300^\circ$ ,  $\theta_2=300^\circ$ ) intramolecular minimum energy state is postulated to be near the active conformation.

The postulated active conformation for **18A** is shown in Figure 10. The observed inhibition potencies of analogues **18B**, **20**, **23**, and **24** of Table 4 can be interpreted in terms of the molecular shape of **1A** in the postulated active conformation. Compound **18B** is active and, therefore, must adopt the postulated active

conformation, or more correctly, active molecular shape, as a low energy stable state. Superposition of **18A** on **18B**, in their respective active molecular shapes, indicates that these two isomers have their indanone rings superimposed, and that their respective piperidine rings are perpendicular to the bicycle and exhibit significant overlapping.

The inactivity of both **23** and **24** is explained by their being too short, due to the lack of a bridging methylene group, to have their indanone and piperidine rings simultaneously superimpose on those of **18A** in the active conformation.

Analogue **20** is only 10–15 times less active than the most active analogue in Table 4(a). It is difficult to explain the lack of higher activity of this compound. One possible explanation for the observed activity profile of **20** is based on the active centers hypothesis of the E2020 derivatives. Compound **20** has two

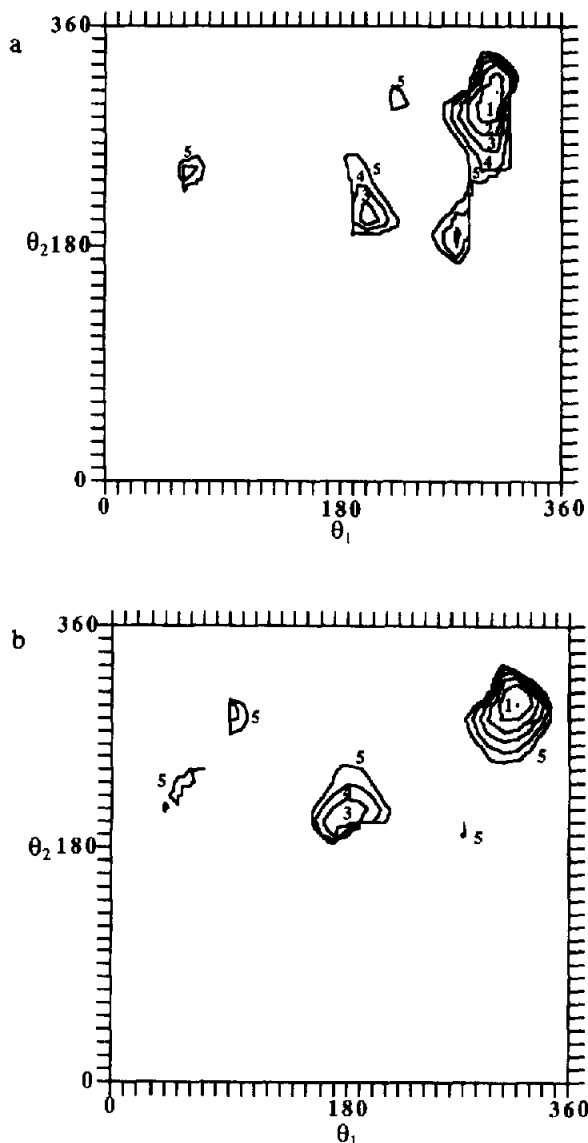


**Figure 8.** Conformational energy maps of key active analogues of **11** from Table 4 used to postulate the active conformation (shape) with respect to ( $\theta_1$ ,  $\theta_2$ ). The energy contours are in kcal per mole relative to the global minimum denoted by (●): (a, top) **18A**, (b, bottom) **20** of Table 4.

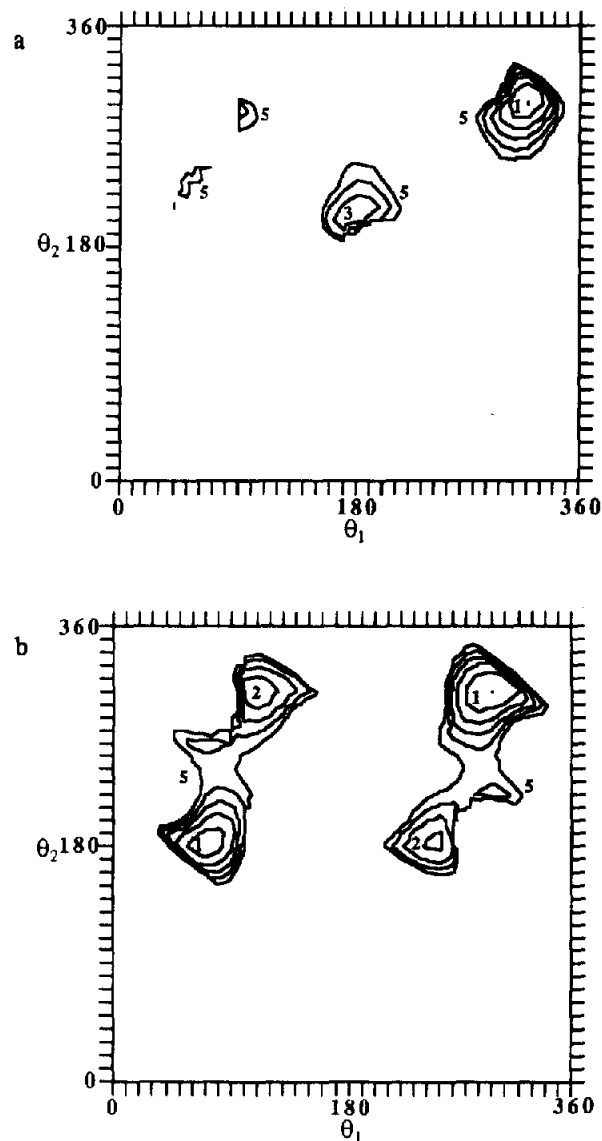


**Figure 9.** Same as Figure 8, but for key inactive analogues (a, top) **21**, (b, bottom) **22** of Table 4.

possible cationic nitrogen centers. The two nitrogens may compete for a single anionic site on the enzyme. These competitive interactions may lead **20** to a binding state for which both N atoms are at similar distances from the anionic receptor center. Such a virtual 'displacement' may then move the carbonyl group of the bicycle from its optimum binding position. A less favorable desolvation binding energy, as compared to **18A/B**, might also contribute to the loss in inhibitory potency.

The absence of a carbonyl oxygen and the relocation of the nitrogen in compounds **22** and **21**, respectively, each lead to major losses in activity. These structural changes also lead to losses in key AChE binding interaction which are discussed in the section on ligand docking.

Hypotheses for the 'active' conformations (shapes) of analogues of **II** having three or four torsion angles ( $W$ ) between the indanone and piperidine rings are not definitive. There are two reasons for this ambiguity. First, the additional conformational flexibility in the three and four torsion angle analogues makes the

exploration of conformational space more difficult. More significant, however, is that inactive three and four torsion angle analogues having structural changes which alter conformational behavior are not available. Hence, the LBA-LCS principle cannot be used.

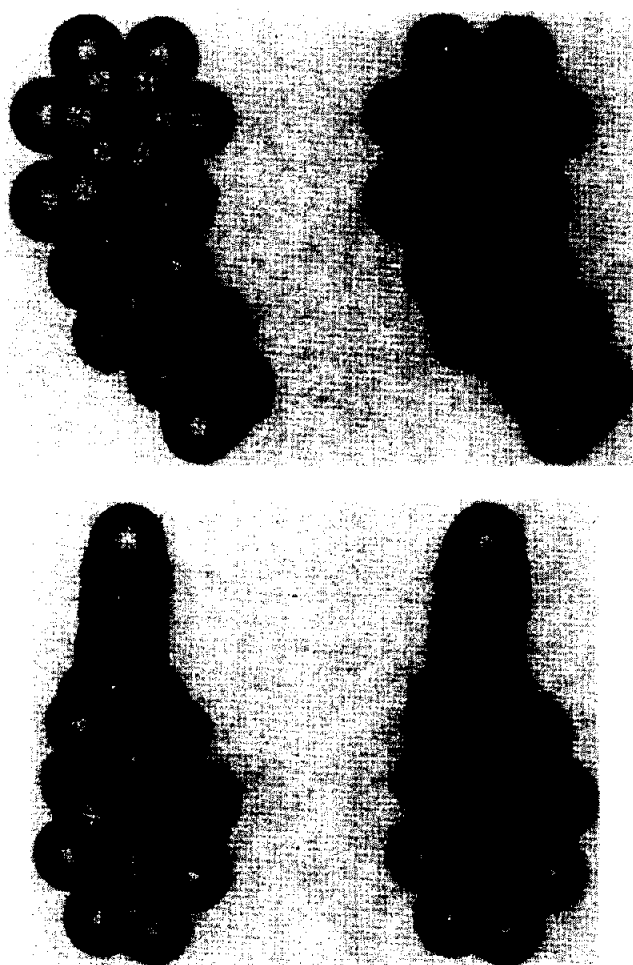
An alternative approach to the LBA-LCS principle to probe for active conformation candidates for the analogues in Table 4(c) first focused on the conformational analysis of the most rigid analogue in this series, compound **29**. The double bonds induce conformational rigidity. All possible combinations of *cis* and *trans* isomers were considered in the conformational analyses of **29**. The all-*trans* conformational energy minima are generally lower than the minima of the other possible isomers by 3–5 kcal/mol. Thus, the assumption was made that the all-*trans*-isomer was the relevant bioactive structure. No all-*trans* structure adopts a minimum energy conformation within 5 kcal/mol of its global intramolecular minimum that permits even marginal similarity superposition of its indanone and piperidine rings onto those of **18A**. It is not possible to determine any energetically reasonable superpositions of the highly flexible analogues **27** and **28** onto **18A**.

The molecular shape analysis becomes more confusing when stable conformations within 5 kcal/mol of the global minimum of each of the two active analogues having three torsions (compounds **25** and **26**) are compared to **18A**, in its active conformation, and to the stable conformations of **29**. In essence, no conformations near the relative minima of **25** or **26** meaningfully superimpose on either **18A** or **29**. One possible explanation of the differences in molecular shapes among the two, three, and four torsion angle classes of analogues of **II** is that each class has a distinct active molecular shape. This explanation is consistent with the docking simulations of E2020 and analogues to AChE that are discussed below.

**Feature 3.** The set of feature 3 derivatives is given in Table 5, and the corresponding model compounds used in the conformational analyses can be represented by **III**.

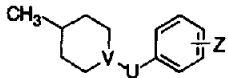
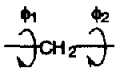
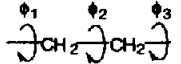
U is most often  $\text{CH}_2$ , but can also be  $\text{C}=\text{O}$  and  $(\text{CH}_2)_2$ . The substituted aromatic ring has also been replaced by cyclohexyl and naphthyl rings. Table 5 has been divided into parts: (a) contains active analogues which have two torsion angles ( $j_1, j_2$ ); (b) contains inactive analogues which have two torsion angles ( $\psi_1, \psi_2$ ); (c) contains a single inactive analogue which has three torsion angles ( $\psi_1, \psi_2, \psi_3$ ).

The LBA-LCS principle was employed to map out the active conformation of the analogues of **III**, reported in Table 5, with respect to  $\phi_1$  and  $\phi_2$ . An analysis of the  $(\phi_1, \phi_2)$  conformational energy maps of the active analogues **30** and **31**, and the inactive analogue **33**, suggests the minimum-energy conformation near  $(\phi_1=200, \phi_2=240^\circ)$  as the active conformation, see Figure 11, the  $(\phi_1, \phi_2)$  map of **30**.

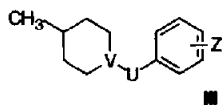


**Figure 10.** The postulated active conformation for analogues of **II** containing two torsion angles ( $\theta_1, \theta_2$ ). The example here is the stereo-view of **18A** of Table 4. (i, top) View into the plane of the indanone ring. (ii, bottom) View along the plane of the indanone ring.

**Table 5.** The analogues of, or similar to, **III** used to map the active conformations, ( $f_1, f_2$ ), with respect to feature 3

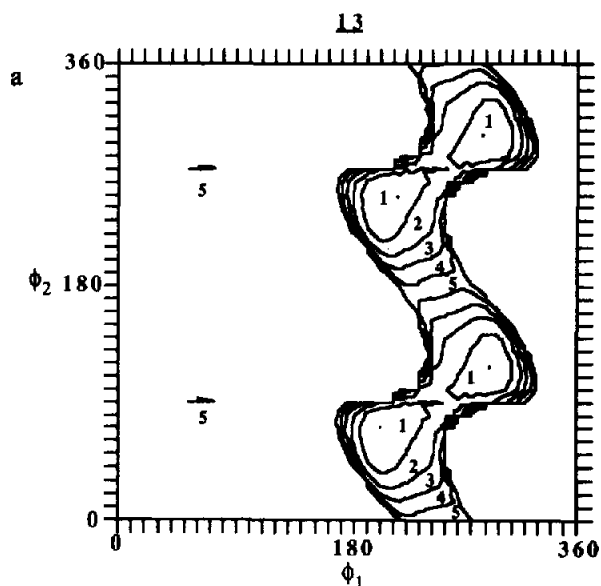
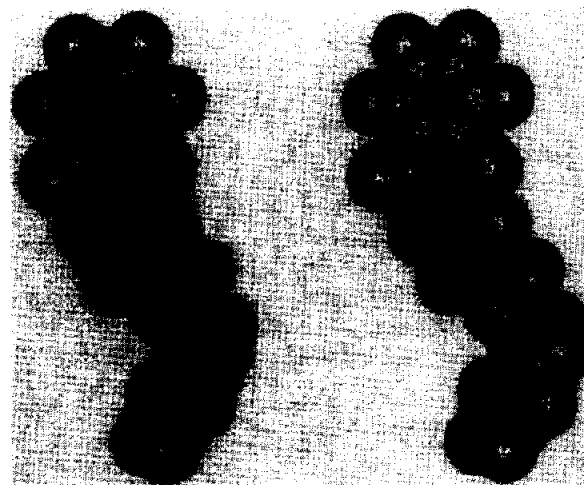
				
No.	U	V	Z	IC <sub>50</sub> (nM)
(a) Active analogues with two torsion angles ( $\phi_1, \phi_2$ )				
30		N	H	5.3
31	-CH <sub>2</sub> -	N	<i>o</i> -CH <sub>3</sub>	10.0
32	-CH <sub>2</sub> -	N	<i>c</i> -C <sub>6</sub> H <sub>11</sub>	8.9
(b) Inactive analogues with two torsion angles ( $\phi_1, \phi_2$ )				
33	-CH <sub>2</sub> -	N	<i>o</i> -NO <sub>2</sub>	160.0
34	-C(O)-	N	H	10000.0
35	-CH <sub>2</sub> -	N	2-naphthyl	2900.0
36	-CH <sub>2</sub> -	N	1-naphthyl	220.0
(c) An inactive analogue with three torsion angles ( $\phi_1, \phi_2, \phi_3$ )				
37		N	H	180.0

<sup>a</sup>IC<sub>50</sub> values correspond to analogues of structure 1.



The overall postulated active conformation for E2020, incorporating feature 3, is shown in Figure 12.

The crystal conformations of the isomers of E2020 (see Fig. 5) are the same as the postulated active conformation with respect to feature 1 ( $\theta_1, \theta_2$ ). However, the

**Figure 11.** The conformational energy map of analogue **30** of Table 5. The energy contours are plotted the same as in Figures 8 and 9. The postulated active conformation is ( $\phi_1 = 200^\circ, \phi_2 = 240^\circ$ ).**Figure 12.** The postulated active conformation of the *R* isomer of E2020.

postulated active conformation differs from the crystal structure with respect to feature 3, ( $\phi_1, \phi_2$ ). The crystal structure adopts the ( $\phi_1 = 300^\circ, \phi_2 = 300^\circ$ ) conformation shown in Figure 11 in contrast to the postulated active conformation of ( $\phi_1 = 200^\circ, \phi_2 = 240^\circ$ ).

The inactive *o,m*-naphthyl analogue **36** has a conformational energy map nearly the same as **33**, thus accounting for its inactivity. However, the conformational energy map of **35**, the inactive *m,p*-naphthyl analogue, is almost identical to that of **30** (active). The inactivity of **35** can only be explained by hypothesizing an intermolecular, sterically forbidden, interaction between part of the *m,p*-naphthyl ring and the receptor wall. This explanation is consistent with the 3-D QSAR developed for substitution onto the phenyl ring in feature 4.

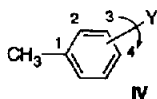
The active analogue **32** and the inactive analogue **34** would both be judged to be inactive based upon their ( $\phi_1, \phi_2$ ) conformation energy profiles. However, these two profiles cannot be directly compared with any of the energy maps of analogues such as **26** and **27** because **32** and **34** possess changes in valence geometry. Nevertheless, the conformational energy minimum found for **32** at ( $\phi_1 = 200^\circ, \phi_2 = 180^\circ$ ), corresponds to the near perfect molecular superposition of **32** onto **30** in its active conformation, thus demonstrating **32** can adopt the postulated active molecular shape.

Compound **34** has a carbonyl group, in contrast to a methylene unit, as the spacer between the piperidine and phenyl rings. None of the conformational minima of **34** can be meaningfully superimposed on the proposed active conformation for **30** or for **31**. This lack of molecular-shape similarity is assumed to be a source for the inactivity of **34**. In addition, the nitrogen atom of the piperidine ring of **34** has a  $sp^2$  hybridization as part of the amide group. Hence, it cannot protonate, and lacks a cationic head.

Finally, the inactivity of **37** of Table 5 can be accounted for by the fact that it does not possess any energetically reasonable intramolecular conformation which corresponds to a molecular shape that is close to the active molecular shape common to the active analogues **30**, **31**, or **32**. In essence, **37** is too 'long' due to the extra methylene spacer.

**Feature 4.** The set of 15 analogues given in Table 6 were used to develop feature 4 3-D QSARs. These E2020 analogues were selected because the only way in which these compounds differ from one another is in the substituent Y. Thus, model compound **IV** was used as the substructure in applying the MDR technique for the feature 4 QSAR analysis.

The range in  $IC_{50}$ s for the 16 analogues is 1–4900 nM. For Y substituents having conformational flexibility, the same molecular modeling and conformational analysis procedures used and referenced in 18 for feature 1 were used to determine the minimum-energy conformer states of Y. Once again, each intramolecular minimum-energy conformer state was used to compute measures of descriptors that are dependent upon substituent conformation. Each descriptor measure was considered in the QSAR analysis.



The following set of descriptors were used as part of the feature 4 QSAR study: (1) The nonoverlap steric volume,  $S_0$ , using the aromatic ring as the molecular superposition criterium. (2) The principle moments of inertia. (3) The center of charge of each analogue. (4) The HOMO energy. (5) The partition coefficient,  $\log P$ , of **IV**.

Trial QSARs were constructed in the same manner as those of feature 1. However, a GFA analysis was not performed.

For feature 4 the optimum 3-D QSAR that could be developed is:

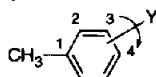
$$-\log (IC_{50}) = -0.107[S_0] + 0.046[IX] - 0.151[HOMO] + 6.683 \quad (3)$$

$$N = 15; R = 0.905; SD = 0.60; F = 16.7.$$

In equation (3)  $S_0$  is the nonoverlap steric volume between each analogue and the shape reference compound (Y=3-OH) and IX is the largest principal moment of inertia of each analogue as represented by **IV**. The shape reference compound was determined by seeing which of the 15 analogues, each tested as the shape reference, gave the statistically most significant QSAR. The values of the QSAR descriptors, the predicted  $-\log(IC_{50})$ s and the corresponding residuals of fit are reported as part of Table 6.

AChE inhibition appears to be less sensitive, with respect to loss in potency, for substitutions onto the indanone ring ( $R_1$ ,  $R_2$ ,  $R_3$ ), as compared to substitutions on the aromatic ring Y. This observation, coupled with the presence of a steric shape term in equation (3), suggests that substructure **IV** is in a more restricted steric environment than **III** when ligand–receptor binding occurs. Loss in inhibition potency seems particularly sensitive to the size of the Y substituent in the *para* position. This trend can be seen in Table 7 where the type and size (steric length) of *para* substituents are reported along with the corresponding  $-\log(IC_{50})$ . Using the unsubstituted ring as a reference, AChE inhibition potency decreases with increasing steric length of the *para* Y substituent. The only exception to this relationship is Y=4-OH, which

Table 6. General SAR data for feature 4 based upon model compound **IV**



No.	Y	$S_0$ ( $\text{\AA}^3$ )	IX	HOMO energy (eV)	Obsd $-\log (IC_{50})$	Calcd $-\log (IC_{50})$	Obsd–calcd $-\log (IC_{50})$
38	3-F	0.86	17.47	–9.549	9.00	8.93	0.07
39	4-OH	6.80	15.24	–8.910	8.74	8.08	0.66
40	3-Me	11.47	23.46	–9.286	8.70	8.02	0.68
41	3-NO <sub>2</sub>	14.06	31.96	–10.342	8.40	8.31	0.09
42	H	0.71	15.72	–9.339	8.28	8.83	–0.55
43	2-F	6.94	26.19	–9.527	8.02	8.67	–0.65
44	4-F	3.69	15.23	–9.478	8.02	8.51	–0.49
45	2-Me	21.40	26.57	–9.262	8.00	7.10	0.90
46	4-NH <sub>2</sub>	9.72	15.47	–8.117	7.44	7.65	–0.21
47	4-Me	17.33	15.72	–9.225	7.40	7.03	0.37
48	4-NO <sub>2</sub>	19.20	22.31	–10.391	7.00	7.32	–0.32
49	3-OMe	18.83	23.55	–8.954	6.66	7.19	–0.53
50	4-OMe	25.37	17.47	–8.895	5.44	6.20	–0.76
51	3,4-OMe	48.19	62.97	–9.198	5.40	5.90	–0.50
52	3,4,5-OMe	70.83	102.57	–9.367	5.31	5.32	–0.01

is also predicted to be less active by equation (3) than is observed (see Table 6).

### Receptor dependent (docking) molecular modeling

**Receptor model.** Sussman and co-workers have reported the crystal structure of AChE from *Torpedo californica* electric organ.<sup>26</sup> The atomic coordinates of AChE were obtained from the Brookhaven Protein Data Bank (PDB entry: 1ACE). Hydrogen atoms were

**Table 7.** *Para* substituents, Y, of feature 4, their steric length (sizes), and observed  $-\log(\text{IC}_{50})$ s

Y	Steric length (Å)	$-\log(\text{IC}_{50})$
H	2.23	8.28
F	2.60	8.02
OH	3.15	8.74
NH <sub>2</sub>	3.20	7.44
CH <sub>3</sub>	3.36	7.40
NO <sub>2</sub>	3.92	7.00
OCH <sub>3</sub>	4.84	5.44

added after deleting the crystalline water molecules present in the X-ray structure, and aliphatic carbon-hydrogen groups were treated as united atoms. Docking studies for an acylated form of the enzyme, EA, were also carried out.<sup>27</sup> The 3-D structure of EA has not been determined so that the EA model used in this study was generated from the X-ray structure of AChE.

AChE which contains 537 amino acids is schematically shown in Figure 13. AChE belongs to the class of  $\alpha/\beta$  proteins and consists of 12  $\beta$ -sheets surrounded by 14  $\alpha$  helices. A close-up view of the enzyme active site from the enzyme surface is shown in Figure 14. The active site serine residue can be seen from the surface of the enzyme. The active site consists of a catalytic triad composed of serine 200, histidine 440 and glutamic acid 327. The catalytic triad lies near the bottom of a long and narrow gorge, which is lined with the side chain rings of fourteen aromatic amino acid residues. These aromatic residues are color-coded orange in Figure 14.



**Figure 13.** Global view of the AChE molecule looking down into the active site gorge.

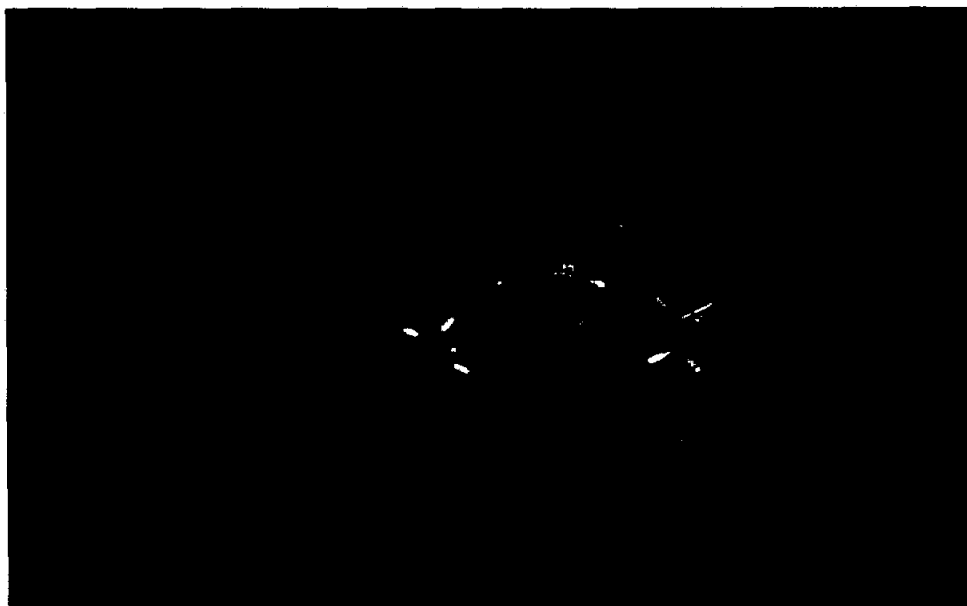


Figure 14. Close-up view of the AChE active site from the enzyme surface.

Figure 15 shows a schematic representation of the enzyme inhibition and the formation of intermediates. Catalysis by AChE involves the active serine residue, and the overall catalytic process proceeds in a three-step mechanism within the catalytic triad.<sup>26</sup> The activated serine residue enables a nucleophilic attack on ACh resulting in hydrolysis and acetate products being released. It is known that some reversible AChE inhibitors show a mixed type of inhibition by blocking the deacetylation process.<sup>28–30</sup> The acetyl group is introduced into the esteratic site in this catalytic process. Therefore, EA can accept an external charged molecule at this vacant anionic site to form an

EA-inhibitor (EAI). Both the *R* and *S* forms of E2020 and THA appear to bind to both the free enzyme and the EA to block both Michaelis complex formation and the deacetylation process.<sup>31</sup>

**Ligand models.** The atomic coordinates of E2020 were taken from its crystal structure, and the other two analogues considered in the docking studies (2A1034, and 2A1050, see Figure 1) were built from E2020. The *S* form of each inhibitor considered in the docking simulation was optimized by the MNDO method. The atomic charges and dipole moments were calculated from these optimized structures. All three analogues

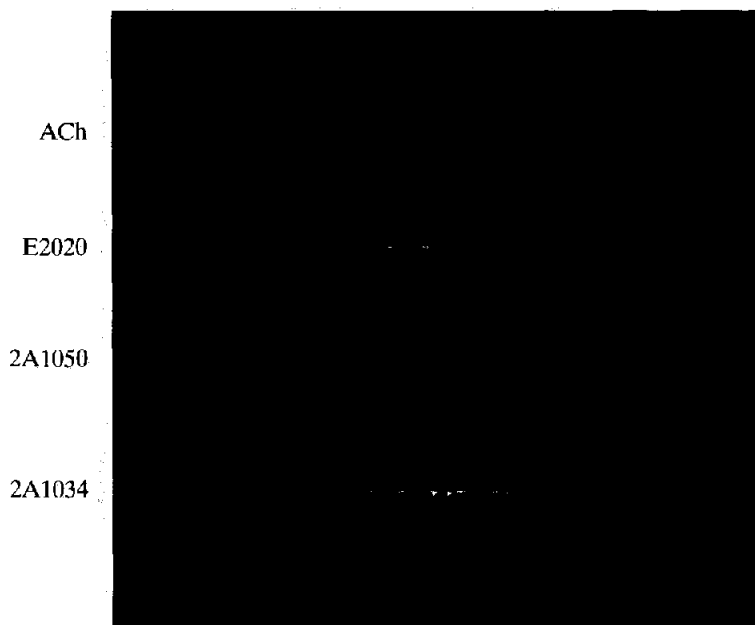


Figure 15. Dipole moments of ACh, E2020, 2A1034, and 2A1050 shown superimposed on the respective molecular structures.

possess large dipole moments, ca. 40–50 debye, and the direction of each dipole runs through the molecule from the benzylpiperidine moiety to the methoxy groups on the indanone ring, see Figure 16. ACh also has a large dipole moment of 23 Debye.

**Docking procedures.** The size of the active-site pocket of AChE is too small for E2020, and its related analogues, to mimic the binding geometry of ACh. Thus, it was necessary to search the long, narrow gorge leading to the active site in AChE for preferred binding locations. A sequential set of search operations were used to determine the enzyme–inhibitor structures and energies. The search operations consisted of: (1) identifying receptor ‘hook’ atoms using CAVHET;<sup>32</sup> (2) construction of initial inhibitor–receptor alignments based upon matching complementary ligand–receptor hook atoms, and the simultaneous alleviation of bad-contact atom-pair interactions by intermolecular ligand translations and rotations coupled with ligand torsion angle rotations; (3) Monte Carlo sampling, using the GREEN docking package,<sup>33</sup> to establish intermolecular low-energy locations and orientations, as well as conformations of the inhibitors, for each initial ligand–receptor model; and (4) molecular dynamics relaxation simulations,<sup>25</sup> using AMBER,<sup>34</sup> of the low-energy complexes generated in the Monte Carlo sampling analyses.

**Docking models of AChE with ACh.** Figure 17 shows a side view of the active site of AChE. The most remarkable feature of this structure is its deep and narrow channel, about 20 Å long and as narrow as 4.5 Å. This gorge penetrates halfway into the enzyme and widens out close to its interior terminus. It has been suggested that the quaternary group of the choline moiety of ACh makes a close contact with the indole ring of Trp 84.<sup>24</sup> However, our docking study indicates that the quaternary moiety of choline binds through

interactions with the  $\pi$  electrons of the aromatic residues in the channel of AChE. Gly 118 and 119 might be part of the oxyanion hole since these glycines make close contacts to the carboxyl oxygen of ACh in the most stable AChE–ACh complex models.

**Docking models of E2020 analogues to AChE and AE.** The docking simulations show that stable conformations are adopted by the inhibitors upon binding to both AChE and acylated AChE. All three inhibitors considered dock to both AChE and the AE in a similar manner. The docking suggests two common features of binding for these compounds: (1) the *N*-benzyl substituent forms a *p*-stacking interaction with the indole side chain of Trp 84 and (2) the piperidine ring locates on the narrowest part of active-site cavity which is formed by four amino acid residues, Tyr 70, Asp72, Tyr 121, and Tyr 334.

E2020 exhibits five key binding interactions (KBI 1–5) involving the methoxy group, the phenyl ring, the carbonyl group in the indanone ring, the protonated nitrogen of piperidine, and the phenyl ring of the benzyl group attached to the nitrogen of piperidine. The carbonyl oxygen interacts with Tyr 121 (KBI 3a) and Tyr (KBI 3b). However, the *S* enantiomer of E2020 ( $k_i=17.5$  nM) only adopts the KBI 3b binding mode. 2A1034 ( $k_i=18.7$  nM) in the *R* form, which is the preferred binding isomer, interacts with the enzyme at only three of these five key sites. 2A1050 ( $k_i=122$  nM) binding involves only two of these interaction sites at the same time for the preferred binding *S* form.

The results of the docking study support the active conformation model discussed above which is characterized by the indanone and piperidine rings being ‘perpendicular’ to one another, where the larger of the two thickness dimensions of the piperidine ring contains its plane relative to the indanone ring.<sup>18</sup> The

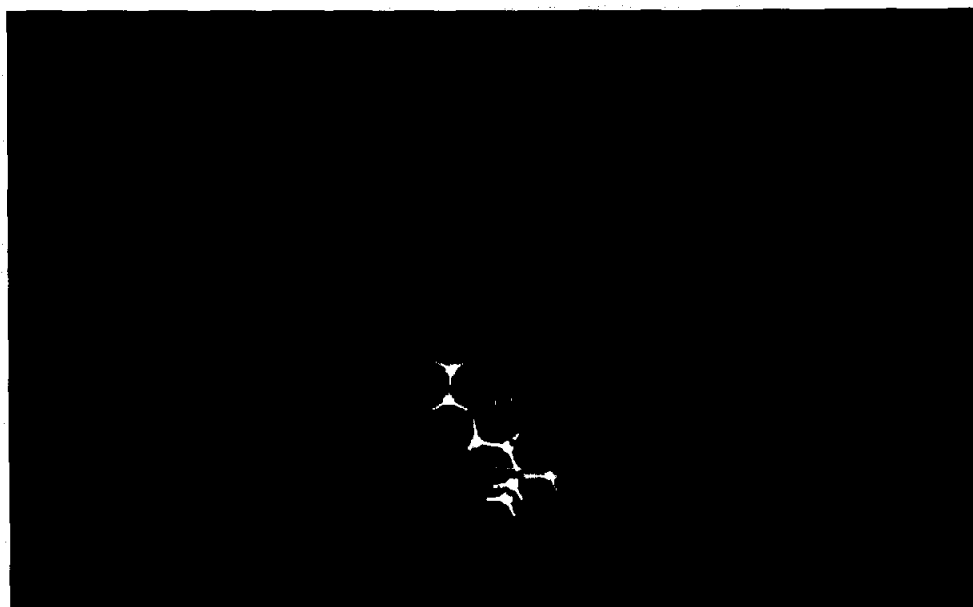


Figure 16. Side view of the AChE active site.

preferred mode of binding of E2020 to AChE is shown in Figure 18. Overall, these results suggest that E2020, and related analogues, are noncovalent AChE inhibitors which bind in the aromatic gorge, but do not interact with the catalytic residues. Consequently, the E2020 analogues can inhibit the Michaelis complex formation step/deacylation step of the hydrolytic reaction of AChE.

### Discussion

QSAR, small molecule X-ray, and molecular modeling methods have been useful in the realization of the E2020 class of AChE inhibitors. These methods have been useful because they have been both functional and appropriate. The capacity to perform individual QSAR, X-ray, and molecular shape analyses quickly, relative to synthetic efforts, and at critical times in the evolution of the research program, are the reasons these methods have been functional. The insight to ask the 'right' questions when employing these methods

has made their use appropriate. We note that not asking questions beyond the scope of a computer-assisted molecular design, CAMD, method qualifies as asking the 'right' question.

The intermolecular docking simulations have complemented the QSAR and molecular shape analyses in providing reasons for the high activity seen in E2020 analogues having differing numbers of spacers groups between the indanone and piperidine rings. E2020 analogues which can adopt long, narrow conformations as low-energy intramolecular states can fit in the long active-site gorge of AChE. The docking simulations indicate that the preferred binding site of E2020 (both isomers) to AChE is not at the ACh active site, but rather some distance away in the channel leading to the active site. This may be the reason E2020 is a potent inhibitor to both AChE and acylated AChE.

In addition, the docking simulations and 3-D QSARs support and reinforce one another. A detailed comparison of the AChE-E2020 docking modes to the

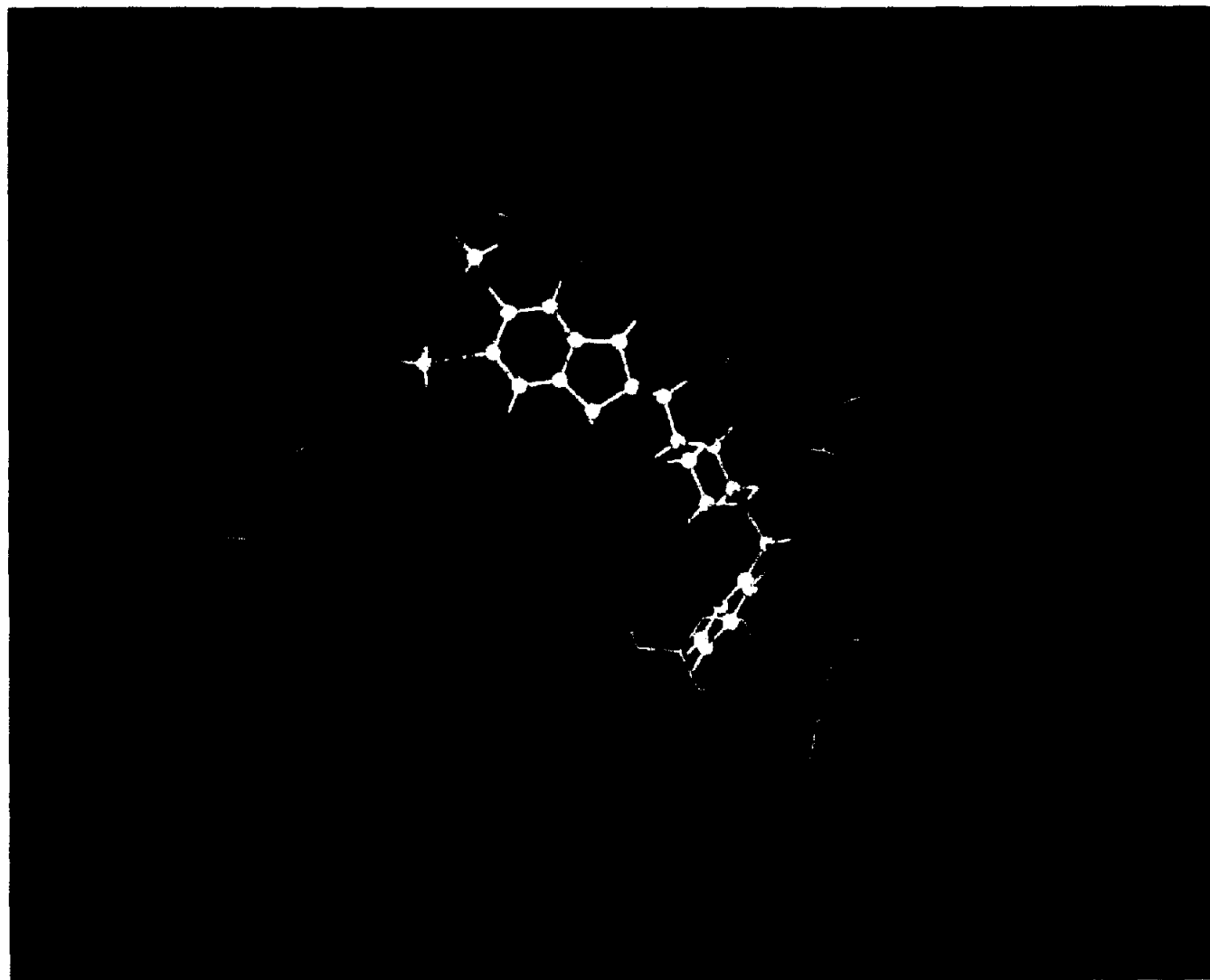


**Figure 17.** Superposition of the *R* and *S* enantiomers of E2020 binding models in the active site cavity with the five key binding interactions (KBIs) defined.

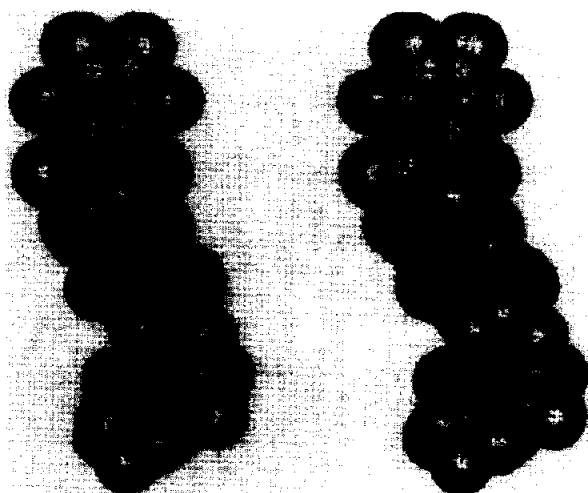


**Figure 18.** The *trans*-decalin analogue superimposed on the *R* enantiomer of E2020 in its postulated active conformation.

descriptor terms in the QSARs [equations (1)–(3)]<sup>25</sup> reveals a self-consistency between sub-binding sites and descriptors. Binding simulations and the use of the QSARs jointly provide a robust tool to predict AChE inhibition activity in new analogues.

There are still pathways to take in the study and understanding of the family of E2020 AChE inhibitors. A better understanding of the geometric binding specificity in the active site channel would enhance inhibitor design capabilities. One measure of success in achieving an insight into inhibitor binding specificity would be to explain the inactivity of what we call the *trans* decalin analogue of E2020 whose structure is shown in Figures 1 and 18. This compound was predicted to be very active as an AChE inhibitor based upon its molecular shape similarity to E2020 (see Figure 18). However, the compound was made and tested and its  $IC_{50}$  was 2530 mM, a quite *inactive* inhibitor. The inactivity was assumed to be due to unfavorable intermolecular binding interactions not identified in the MSA study. At the time of the MSA study the AChE crystal structure was not available. Recent docking simulations of the *trans*-decalin analogue to AChE, carried out in the same manner as for E2020 and some of its other analogues and described above, also suggests it should be a potent inhibitor. Thus, future molecular modeling studies, and, in particular, docking simulations of the E2020 family of AChE inhibitors should keep the understanding of the low-activity of the *trans*-decalin analogue as both a goal and a corresponding measure of success.

Docking simulations may provide some guidelines for structural changes in the four features of E2020. A primary target for structural changes may be the indanone ring. There are other bicycles that lead to active analogues<sup>18</sup> suggesting a structure–activity mapping may be possible by docking simulation.

Implementation of docking simulations in a design mode is predicated upon reliable calculations. The

ability to predict reliable and accurate ligand–receptor binding energies remains elusive in intermolecular modeling. Perhaps the best chances for success in the E2020 analogue–AChE docking simulations is to combine X-ray studies to elucidate AChE–inhibitor complex geometries with free-energy force-field refinement<sup>35</sup> docking simulations. The X-ray structures can provide realistic initial geometries to the docking simulations for a training set of inhibitors for which the inhibition potencies have been measured. The terms in the force field used to compute the binding energies of the inhibitors are then scaled, in a QSAR fashion, to establish a correlation between inhibition potency and binding free energy.

Overall, the E2020 project has had a successful past in terms of CAMD applications and there is every reason to believe in a bright future.

### Acknowledgments

AJH is grateful for the financial support of Eisai for some parts of the work reported here. Mario Cardozo has been a major contributor to some of the QSAR studies (features 1 and 4) and the conformational and molecular shape analyses (features 2 and 3). We also appreciate the helpful discussions with S. Nochi of Eisai Co., Ltd.

### References and Notes

1. Yamanishi, Y.; Ogura, H.; Kosasa, K.; Araki, S.; Sawa, Y.; Yamatsu, K. *Basic Clinical, and Therapeutic Aspects of Alzheimer's and Parkinson's Diseases*; Plenum: New York, 1990; Vol. 2, pp 409–413.
2. Bartus, R. T.; Dean, III, R. L.; Beer, B.; Lippa, A. S. *Science* **1982**, 217, 408.
3. Sims, N. R.; Bowen, D. M.; Allen, S. J.; Tomalson, C. C. T.; Neary, D.; Thomas, D. J.; Davison, A. N. *J. Neurochem.* **1983**, 40, 503.
4. Gottfries, C. G. *Psychopharmacology* **1985**, 86, 245.
5. Perry, E. K. *Br. Med. Bull.* **1986**, 42, 63.
6. Hulme, E. C.; Birdsall, N. J. M.; Buckley, N. J. *Annu. Rev. Pharmacol. Toxicol.* **1990**, 30, 633.
7. Yamanishi, Y.; Ogura, H.; Kosasa, K.; Araki, S.; Sawa, Y.; Yamatsu, K. *Basic Clinical, and Therapeutic Aspects of Alzheimer's and Parkinson's Diseases*; Plenum: New York, 1990; Vol. 2, p 409.
8. Sugimoto, H.; Tsuchiya, Y.; Sugumi, H.; Higurashi, K.; Karibe, N.; Iimura, Y.; Sasaki, A.; Kawakami, Y.; Nakamura, T.; Araki, S.; Yamanishi, Y. *J. Med. Chem.* **1990**, 33, 1880.
9. Nochi, S. unpublished results.
10. Homma, A.; Hasegawa, K.; Nishimura, T.; Kameyama, M.; Hariguchi, S.; Imai, Y. In *proceedings of 6th Congress of the International Psychogeriatric Association*, 1993.
11. Summers, W. K.; Koehler, A. L.; Marsh, A. M.; Tachiki, K.; Kling, A. *Lancet* **1989**, 729.
12. Ishihara, Y.; Hirai, K.; Miyamoto, M.; Goto, G. *J. Med. Chem.* **1994**, 37, 2292.

13. Villalobos, A.; Blake, J.F.; Biggers, C.K.; Butler, T. W.; Chapin, D. S.; Chen, Y. L.; Ives, J. L.; Jones, S. B.; Liston, D. R.; Nage, A. A.; Nason, D. M.; Nielsen, J. A.; Shalaby, I. A.; White, W. F. *J. Med. Chem.* **1994**, *37*, 2721.
14. Dewar, M. J. S.; Thiel, W. J. *Am. Chem. Soc.* **1977**, *99*, 4899.
15. Hulme, E. C.; Birdsall, N. J. M.; Buckley, N. J. *Annu. Rev. Pharmacol. Toxicol.* **1990**, *30*, 633.
16. Johnson, C. K., *ORTEP II*. Report ORNL-5138. Oak Ridge National Laboratory, Tennessee, U.S.A.
17. Hopfinger, A. J.; Malhotra, D.; Battershell, R. D.; Ho, A.; and Chen, J. A. *Pest. Sci.* **1984**, *9*, 631.
- 18 (a) Cardozo, M. G.; Iimura, Y.; Sugimoto, H.; Yamanishi, Y.; Hopfinger, A. J. *J. Med. Chem.* **1992**, *35*, 584. (b) Cardozo, M. G.; Kawai, T.; Iimura, Y.; Sugimoto, H.; Yamanishi, Y.; Hopfinger, A. J. *J. Med. Chem.* **1992**, *35*, 590.
19. Rhyu, K.-B.; Patel, H. C.; Hopfinger, A. J. *J. Chem. Inf. Comput. Sci.* **1995**, *35*, 771.
20. Medicinal Chemistry Software, *Medchem Software Manual, Release 3.51*; Pomona College: Claremont, California, April 1987.
21. *SAS User's Guide: Basics, SAS Release 5.18*; SAS Institute, Inc.: Cary, North Carolina, 1986.
22. Holland, J. *Adaptation in Artificial and Natural Systems*; University of Michigan: Ann Arbor, 1975.
23. Rogers, D.; Hopfinger, A. J. *J. Chem. Inf. Comput. Sci.* **1994**, *34*, 854.
24. Hopfinger, A. J.; Burke, B. J. In *3-D QSAR in Drug Design-Theory, Methods and Applications*, Kubinyi, H., Ed.; ESCOM Science: Leiden, 1993; pp 276-306.
25. Burke, B. J. Ph.D. Thesis, University of Illinois at Chicago, Illinois, 1992.
26. Sussman, J. L.; Harel, M.; Frolow, F.; Offner, C.; Goldman, A.; Toker, L.; Silman, I. *Science* **1991**, *253*, 872.
27. Inoue, A.; Kawai, T.; Wakita, M.; Iimura, Y.; Sugimoto, H.; Kawakami, Y., *J. Med. Chem.*, submitted.
28. Krupka, R. M.; Laidler, K. J. *J. Am. Chem. Soc.* **1961**, *83*, 1445.
29. Krupka, R. M.; Laidler, K. J. *J. Am. Chem. Soc.* **1961**, *83*, 1454.
30. Krupka, R. M. *Biochemistry* **1965**, *4*, 429.
31. Nochi, S.; Asakawa, N.; Sato, T. *Biol. Pharm. Bull.* **1995**, *18*, 1145.
32. CAVHET is in the original program developed by A. Inoue.
33. Tomioka, N.; Itai, A. *J. Comput-Aided Mol. Design* **1994**, *8*, 347.
34. Weiner, S. J.; Kollman, P. A. *J. Comp. Chem.* **1986**, *7*, 230.
35. Hopfinger, A. J.; Tokarski, J. *J. Chem. Inf. Comput. Sci.*, submitted.

(Received in U.S.A. 5 October 1995)